Journal of Power Sources 262 (2014) 104–111

Contents lists available at ScienceDirect

Journal of Power Sources

journal homepage: www.elsevier.com/locate/jpowsour

Crystal structure and multicomponent effects in $Li_{1+x}Mn_{2-x-y}Al_yO_4$ cathode materials for Li-ion batteries

Fu-Da Yu [a,c], Zhen-Bo Wang [a,*], Fei Chen [a], Jin Wu [b], Xiao-Gang Zhang [b], Da-Ming Gu [c]

[a] School of Chemical Engineering and Technology, Harbin Institute of Technology, No. 92 West-Da Zhi Street, Harbin 150001, China
[b] Xi'an Huijie Industrial Co., Ltd., Xi'an 710116, China
[c] School of Science, Harbin Institute of Technology, No. 92 West-Da Zhi Street, Harbin 150001, China

HIGHLIGHTS

- Li, Al co-doped $LiMn_2O_4$ was synthesized using industrial raw materials in bulk scale (>20 kg).
- Li, Al co-doping significantly changed the unit cell parameter and atomic arrangement.
- The expansion of LiO_4 tetrahedron and contraction of MO_6 octahedron were identified by Rietveld refinement of XRD.
- The optimized composition is $Li_{1.06}Mn_{1.86}Al_{0.08}O_4$ with high-rate performance and good structure-stabilization.
- $Li_{1.06}Mn_{1.86}Al_{0.08}O_4$ has capacities of 91 mAh g^{-1} at 0.5 C and of 88 mAh g^{-1} at 10 C at 55 °C after 200 cycles.

GRAPHICAL ABSTRACT

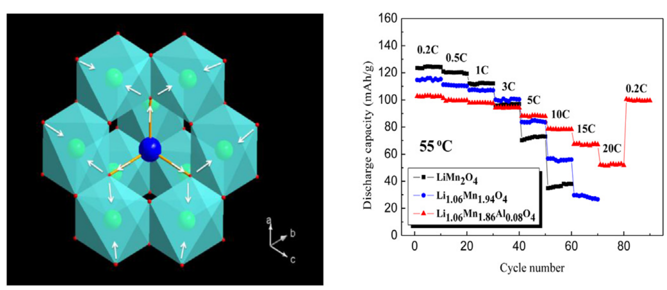

ARTICLE INFO

Article history:
Received 7 February 2014
Received in revised form
10 March 2014
Accepted 24 March 2014
Available online 1 April 2014

Keywords:
Spinel lithium manganese oxide
Doping
Crystal structure
Electrochemical property

ABSTRACT

Li, Al co-doped $LiMn_2O_4$ ($Li_{1+x}Mn_{2-x-y}Al_yO_4$, $0 \leq x \leq 0.12$, $0 \leq y \leq 0.1$) cathode has been synthesized via a solid-state reaction designedly using industrial raw materials in bulk scale (>20 kg). The multicomponent substitution effects on the crystal structures are examined systematically by Rietveld refinement of X-ray diffraction, and the resultant electrochemical properties for Li-ion batteries are also evaluated by galvanostatic charge–discharge and electrochemical impedance spectroscopy measurements. As a result, Li, Al co-doping significantly changes the unit cell parameter and atomic arrangement. With the increasing of doping levels, a cell dimension contracts with concomitant changes in bond length, whereby the MO_6 octahedron (M = Mn/Li/Al) shrinks to provide structural integrity and the LiO_4 tetrahedron expands to facilitate a fast electrochemical process. The strong spinel-framework contributes to a better structure-stabilization, resulting in a superior capacity retention ratio of 90% after 200 cycles at 0.5 C at 55 °C for the optimized composition ($Li_{1.06}Mn_{1.86}Al_{0.08}O_4$), which possesses an initial value of 102 mAh g^{-1}. Meanwhile, the expansion of LiO_4 tetrahedron leads to better high-rate performance, bringing about a capacity of 88 mAh g^{-1} upon cycling at 10 C at 55 °C. Further, $Li_{1.06}Mn_{1.86}Al_{0.08}O_4$ displays lower impedance than that of the pristine $LiMn_2O_4$.

* Corresponding author. Tel.: +86 451 86417853; fax: +86 451 86418616.
E-mail address: wangzhb@hit.edu.cn (Z.-B. Wang).

http://dx.doi.org/10.1016/j.jpowsour.2014.03.120
0378-7753/

1. Introduction

Up to the present, lithium-ion batteries (LIBs) are indispensable power sources for portable equipment, and for their potential applications in electric vehicles and energy storage systems, the safety concerns should be more seriously cared [1–3]. Spinel lithium manganese oxides ($LiMn_2O_4$) with 3D tunnel structure for the migration of Li^+ ions have been supposed to be a promising candidate for cathode materials, given that they can provide a reliable degree of safety and are cost-effective, compared to layered cathode materials, such as $LiCoO_2$ and $LiNi_xCo_yMn_zO_2$ [4,5]. However, spinel $LiMn_2O_4$ remains a persistent deficiency which is prone to severe capacity fade at elevated temperatures (50–60 °C), being attributed to the formation of Mn^{2+} ions takes place through Jahn-Teller active Mn^{3+} ions which are easier to decompose at higher temperatures [6–8].

Taking into account that Mn dissolution occurs at the electrode/electrolyte interface, one strategy that has been employed to combat this stability issue has been to minimize the electrode/electrolyte contact through creating a coating layer [9–12]. Although a protection layer has been proven effective in most cases, the uniform or compact of prepared layers is highly sensitive to the synthesis conditions, as well as the cost of the additional coating process, becoming the impediments for wide-spread use of $LiMn_2O_4$. On the other hand, to tackle this point of capacity fade, numerous efforts have been devoted to partially substitute other metal ions for manganese in the crystal structure, which leads to better cyclability at elevated temperatures. Doping can have a direct impact on the structure and stability of $LiMn_2O_4$ during lithium extraction/insertion. Some transition and non-transition metal elements, Such as Cr [13], Fe [14], Mg [15], Co [16], Ni [17], Cu [18], Bi [19], Sn [20], Ru [21], Al [22] and Li [23], have been substituted to stabilize the spinel structure and/or provide facile charge transport.

The doping approach by substituting with electroinactive elements [15,19,20,22,23] has been considered as an effective avenue, which is based on the idea that the dopant ions increase the average valence state of Mn to be higher than +3.5, expecting a mitigation of structural distortion by the Jahn-Teller, being induced by the strong metal-oxygen bonding of the substituted metal ion. In most cases, structural stabilization, minimized polarization, and improved electrical conductivity were obtained via a substitution with low doping levels. As far as the stability at high temperatures is concerned, however, $LiMn_2O_4$-based compounds still require significant improvement.

Dual metal element doping has also been found effective in improving the cycling performance of $LiMn_2O_4$. Prior work has revealed that doping of Al and the inclusion of additional Li can improve notably the thermal stability of $LiMn_2O_4$ [24]. It is enunciated the interaction energies of $LiMn_2O_4$ increase by employing Li, Al co-dopants into the spinel structure through an isothermal calorimetry study. However, more details of the content and structural analysis results of the dopants must be given for understanding the relationship between the atomic arrangements and the resultant electrochemical properties, particularly at elevated temperatures. Besides, the doping inevitably compromises the maximal capacity attainable by doped-$LiMn_2O_4$. In this regard, an optimum proposal of doping is needed to pursue a higher rate capability, thus the superior capacity retention based on the better structure-stabilization could compensate the lower original capacity.

Herein, we synthesized $Li_{1+x}Mn_{2-x-y}Al_yO_4$ spinels via a simple solid-state reaction designedly using industrial raw materials in bulk scale (>20 kg). The aim is to present the detail of multicomponent effects on the crystal structure, linking to the unit cell dimension, atomic content and arrangements, which are directly related to the significant improvement of electrochemical performance of Li, Al co-doped $LiMn_2O_4$. We show that the volume changes of LiO_4 tetrahedron and MO_6 octahedron (M = Mn/Li/Al), thus, unit cell contraction and suppression of a two-phase region, by incorporating Li^+, Al^{3+} co-dopants into the spinel lattice are responsible for the superior cyclability and rate performance of $Li_{1+x}Mn_{2-x-y}Al_yO_4$. In this multicomponent system, the structure-property relationship of the $Li_{1+x}Mn_{2-x-y}Al_yO_4$ is revealed, as a way to optimize the behavior of these cathodes.

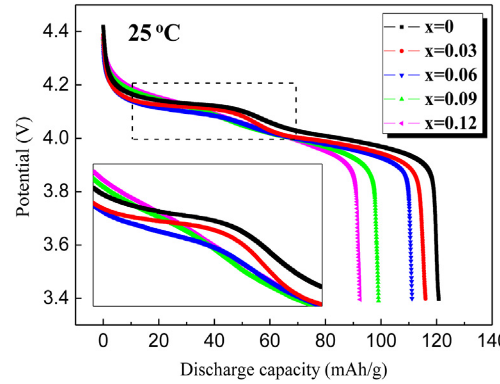

Fig. 1. The initial discharge curves of the $Li_{1+x}Mn_{2-x}O_4$ samples with cycling at 0.5 C at 25 °C.

2. Experimental

2.1. Fabrication of materials

$Li_{1+x}Mn_{2-x-y}Al_yO_4$ spinels were synthesized via a simple conventional solid-state reaction. All reagents used were of industrial raw materials without further purification. Required amounts of Li_2CO_3, electrolytic MnO_2, and Al_2O_3 were dry grinded in the ball mill for 30 min, then the mixture was heated at 600 °C for 6 h and 750 °C for 12 h in air, and followed by furnace cooling to produce the final spinel sample. For comparison purposes, stoichiometric $LiMn_2O_4$ and Al-undoped Li-excess $Li_{1+x}Mn_{2-x}O_4$ spinels were also prepared by the similar method as described above with the stoichiometric amounts of Li/Mn and without the addition of Al_2O_3, respectively. A typical batch size was >20 kg.

2.2. Physicochemical characterizations

Sample crystallographic phase identification was investigated by X-ray power diffraction (XRD) method utilizing a Shimadzu-9100 with Cu Kα radiation (λ = 1.54056 Å) at room temperature, under Bragg–Brentano geometry in the 2θ range of

Table 1
The lattice parameters and the ratio of Li/(Li + Mn) in the $Li_{1+x}Mn_{2-x}O_4$ samples.

Sample	Lattice parameter (Å)	Stoichiometric ratio of Li/(Li + Mn)	Measured ratio of Li/(Li + Mn)
$x = 0$	8.247	0.333	0.332
$x = 0.03$	8.242	0.343	0.341
$x = 0.06$	8.235	0.353	0.352
$x = 0.09$	8.229	0.363	0.363
$x = 0.12$	8.223	0.373	0.372

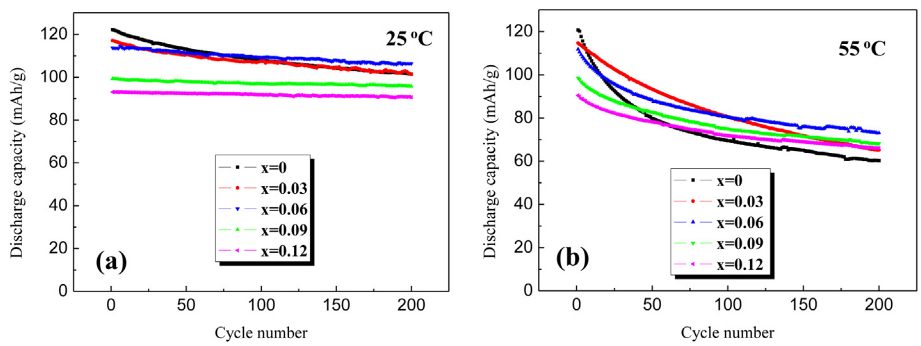

Fig. 2. The cycling performance of the $Li_{1+x}Mn_{2-x}O_4$ samples with cycling at 0.5 C (a) at 25 °C and (b) at 55 °C.

15–120° at an interval of 0.02°, with a counting time duration of 10 s for each step. The lattice parameters were refined by the Rietveld method with General Structure Analysis Software (GSAS program) [25]. Surface morphology of the sample was observed by scanning electron microscope (SEM) using a Quanta-200. The size distribution of the sample was determined using a Beckman laser particle size analyzer and the tap-density was examined using a tapping apparatus (FZS4-4B). Compositional characterization was carried out by inductively coupled plasma-atomic emission spectrometer (ICP-AES). The relative standard deviation of the replicated measurements by ICP-AES and the recovery of the calibration solutions did not exceed 1%, relatively.

The electrochemical tests were carried out in coin-type cells (CR 2025) with lithium metal counter electrodes. The cells were assembled in an argon-filled glove box. Cathode slurries were prepared by mixing the active material, conductive acetylene black and polyvinylidene fluoride (PVDF) in an 80:10:10 wt% in 1-methyl-3-pyrrolidone (NMP) solvent. These slurries were then cast onto an aluminum foil and dried at 120 °C in a vacuum oven for 12 h. Then the foil was punched into circular electrode 1.4 cm in diameter. Its loading weight was approximately 2 mg cm^{-2}. The electrolyte was 1 mol L^{-1} $LiPF_6$ dissolved in a 1:1 vol% of ethylene carbonate (EC) and dimethyl carbonate (DMC). The charge–discharge tests were performed on a NEWWARE battery tester. Electrochemical impendence spectroscope (EIS) measurements were performed on a CHI650D electrochemical workstation, which conducted with AC amplitude of 5 mV in the frequency range from 10^5 Hz to 0.01 Hz.

3. Results and discussion

3.1. Stoichiometric $LiMn_2O_4$ and Li-excess $Li_{1+x}Mn_{2-x}O_4$ spinels

In order to understand the effectiveness of Li-dopant on the electrochemical properties of stoichiometric $LiMn_2O_4$, Fig. 1 compares discharge curves of stoichiometric $LiMn_2O_4$ and Li-excess $Li_{1+x}Mn_{2-x}O_4$ samples cycled at 0.5 C at room temperature (25 °C). The Li-excess samples, where $x = 0.03, 0.06, 0.09, 0.12$, were measured by the ICP-AES analysis, as shown in Table 1. It is not unexpected that the ICP-AES measured compositions indicating slight Li losses during synthesis, but it still brings about a good match to the expected molar ratio. The stoichiometric sample presents two distinguished charge/discharge plateaus, revealing a two-step process for $LiMn_2O_4$ during Li^+ ions intercalation/deintercalation. The step is gradually less pronounced in the $Li_{1.03}Mn_{1.97}O_4$ and $Li_{1.06}Mn_{1.94}O_4$ samples, indicating the Li-doping could alleviate the long-range ordering of the Li^+ ions in the spinel $LiMn_2O_4$ [26,27]. Moreover, for the samples with higher doping levels ($Li_{1.09}Mn_{1.91}O_4$ and $Li_{1.12}Mn_{1.88}O_4$), as shown in the inset, the voltage step is essentially fully suppressed.

Fig. 2(a) shows the cycling performance of the five samples cycled at 25 °C at 0.5 C. From Fig. 2(a) it can be concluded that doping inevitably reduces the maximal capacity attainable, but after 200 cycles of charging/discharging, the $Li_{1.06}Mn_{1.94}O_4$ sample delivers a higher capacity of 106.5 mAh g^{-1} than that of stoichiometric $LiMn_2O_4$ sample, the latter is yielding a capacity of 101.4 mAh g^{-1}. The capacity retentions of the stoichiometric $LiMn_2O_4$, Li-excess $Li_{1.03}Mn_{1.97}O_4$, $Li_{1.06}Mn_{1.94}O_4$, $Li_{1.09}Mn_{1.91}O_4$ and $Li_{1.12}Mn_{1.88}O_4$ samples are 83.0%, 86.6%, 93.6%, 96.5% and 97.5%, respectively, after 200 cycles. The effectiveness of structure-stabilization by Li-doping was also confirmed at 55 °C. As shown in Fig. 2(b), the capacities of 60.4, 65.3, 73.1, 68.4 and 66.4 mAh g^{-1} are obtained for the five above-mentioned samples, respectively. Moreover, the capacity retentions of the five samples are 50.2%, 56.9%, 65.3%, 69.2% and 73.6%, respectively, after 200 cycles. These results indicate that the Li-doping could efficiently suppress the ordering of Li^+ ions and improve the stability of the spinel structure.

Therefore, in order to study the changes in crystal structure of stoichiometric $LiMn_2O_4$ and Li-excess $Li_{1+x}Mn_{2-x}O_4$ spinels, the samples were carefully examined by XRD method. Fig. 3 shows the XRD patterns of the samples, corresponding with the JCPDS card No. 35-0782. The diffraction peaks of all the samples could be unambiguously indexed as cubic spinel structure with an *Fd-3m* space group and without any impurities, except the $Li_{1.12}Mn_{1.88}O_4$ sample, which shows the characteristic patterns of Li_2MnO_3 phase (JCPDS: 01-084-1634), probably due to the heavily doping of Li into the spinel $LiMn_2O_4$ [28]. The cubic lattice parameters of the spinel phase calculated from the diffraction data are shown in Table 1. From Table 1, it can be concluded that the cell size decreases with increasing *x*, which is mainly due to the Li-doping into the spinel

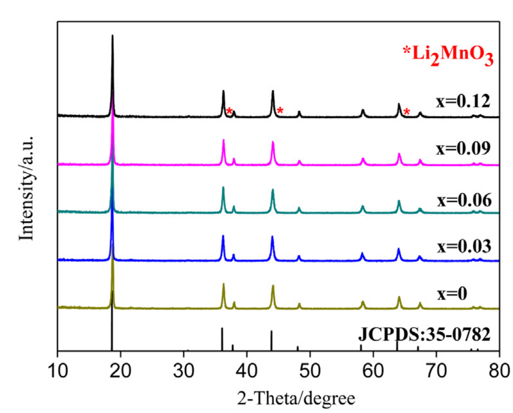

Fig. 3. X-ray diffraction patterns of $Li_{1+x}Mn_{2-x}O_4$ samples.

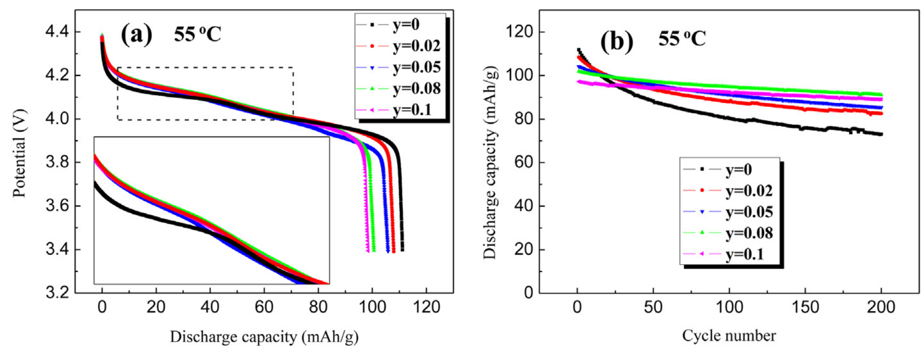

Fig. 4. (a) The initial discharge curves of the $Li_{1.06}Mn_{1.94-y}Al_yO_4$ samples with cycling at 0.5 C at 55 °C; (b) The cycling performance of the $Li_{1.06}Mn_{1.94-y}Al_yO_4$ samples with cycling at 0.5 C (a) at 25 °C and (b) at 55 °C.

structure to form a $Li[Li_xMn_{2-x}]O_4$ composite. The Li^+ ions dope into the octahedral sites in the spinel structure, leading to the decrease in content of Mn^{3+} ion and the increase in content of the Mn^{4+} ion to keep the charge balance. The radius of the Mn^{4+} ion (0.54 Å) is smaller than that of the Mn^{3+} ion (0.65 Å) [29], so the increase of Mn^{4+}/Mn^{3+} ratio in the spinel reduces the lattice size. As we know, the gravimetric capacity of $LiMn_2O_4$ is inversely proportional to the average Mn oxidation state, so the composition of

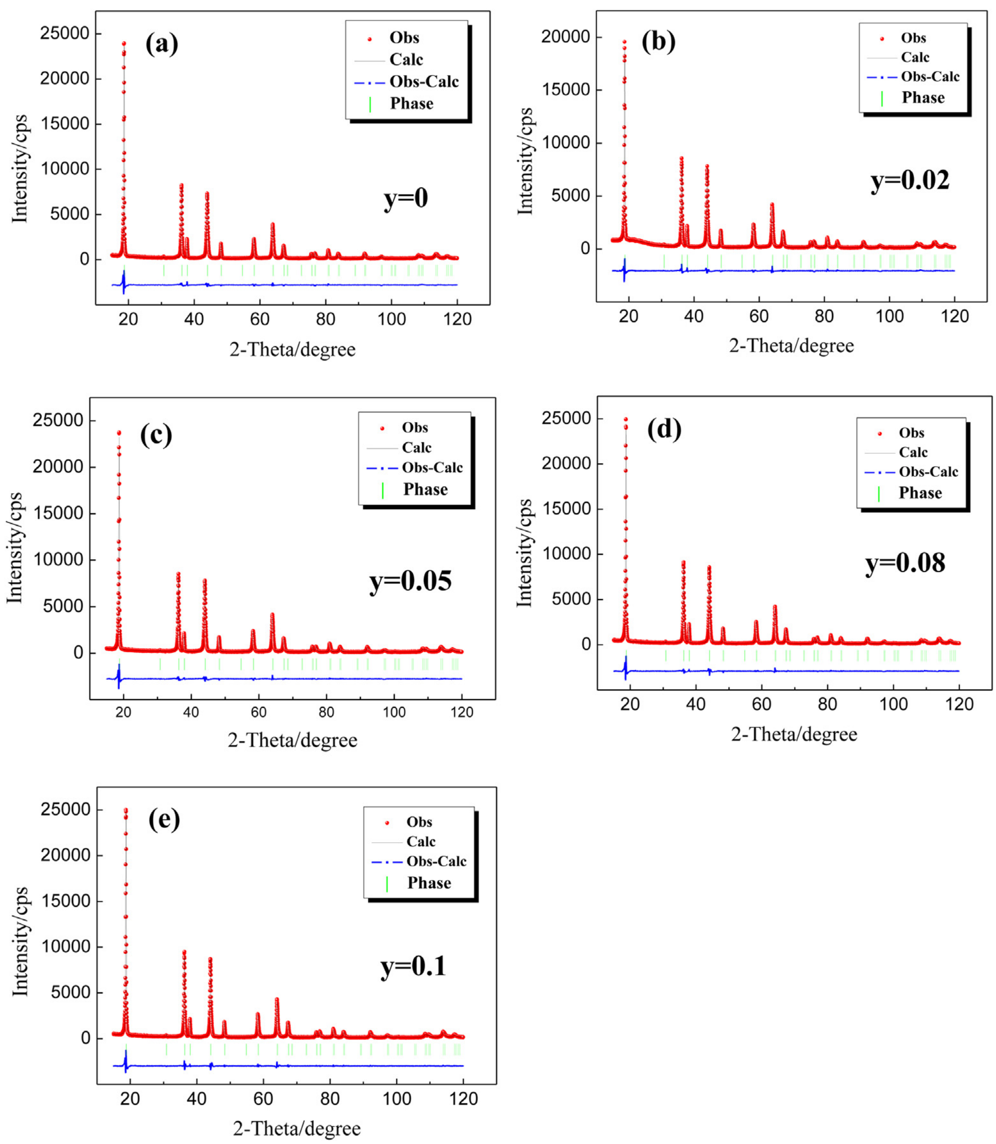

Fig. 5. Rietveld refinement patterns using powder X-ray diffraction of the $Li_{1.06}Mn_{1.94-y}Al_yO_4$ samples. The dot marks show observed X-ray diffraction intensities, the red line represents calculated intensities, the blue line at the bottom is the difference between the calculated and observed intensities, and the green tick marks above the difference plot show the position of the Bragg peaks. (For interpretation of the references to color in this figure legend, the reader is referred to the web version of this article).

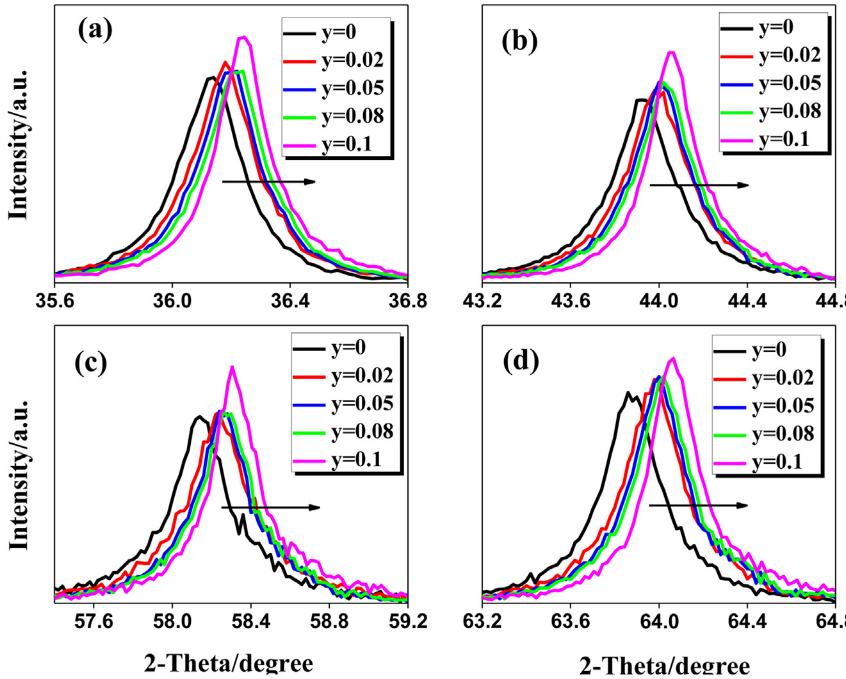

Fig. 6. Expanded 2θ region of the X-ray diffraction patterns of the $Li_{1.06}Mn_{1.94-y}Al_yO_4$ samples.

the sample was optimized to $Li_{1.06}Mn_{1.94}O_4$. Furthermore, it is worthy mention that, the statement of the additional Li has been incorporated into the crystal lattice, forming a non-stoichiometric Li-excess spinel, would be described in further detail below.

3.2. The electrochemical and structural properties of the $Li_{1.06}Mn_{1.94-y}Al_yO_4$ samples

To further optimize the electrochemical performance of Li-doped $LiMn_2O_4$ at elevated temperatures, the effects of Al-doping on the $Li_{1.06}Mn_{1.94}O_4$ samples have been investigated. From Fig. 4(a) it can be observed that suppression of a two-phase region of $Li_{1.06}Mn_{1.94}O_4$ sample by Al-doping, which is in good agreement with the above discussions. Moreover, the discharge capacity changes of $Li_{1.06}Mn_{1.94-y}Al_yO_4$ with cycling at 0.5 C at 55 °C can be seen in Fig. 4(b). The inferior capacity retention of $Li_{1.06}Mn_{1.94}O_4$ (maintaining 65.3% after 200 cycles) was significantly improved by Al-doping, resulting in 76.2%, 82.0%, 89.5%, and 91.7% for $y = 0.02$, 0.05, 0.08, and 0.1, respectively. These Al-undoped $Li_{1.06}Mn_{1.94}O_4$ and Al-doped $Li_{1.06}Mn_{1.94}O_4$ samples deliver capacities of 73.1, 82.6,

Table 2
Summary of structural refinement of the $Li_{1.06}Mn_{1.94-y}Al_yO_4$ samples by a Rietveld method using a Cubic *Fd-3m* space group[a].

Sample	Atom site	$x = y = z$	Occupancy	Lattice parameter a (Å)	Interatomic distance (Å)		Reliability factors		
					$[Li]_{8a}$–$[O]_{32e}$	$[M]_{16d}$–$[O]_{32e}$	R_p/%	R_{wp}/%	χ^2
$y = 0$	$[Li]_{8a}$	0.1250	1.0000	8.2352(9)	1.8346(5)	2.0321(3)	6.74	9.02	3.47
	$[Mn]_{16d}$	0.5000	0.9726						
	$[Li]_{16d}$	0.5000	0.0275						
	$[Al]_{16d}$	–	–						
	$[O]_{32e}$	0.2592(5)	1.0000						
$y = 0.02$	$[Li]_{8a}$	0.1250	1.0000	8.2324(7)	1.8792(4)	2.0019(7)	5.70	7.44	2.59
	$[Mn]_{16d}$	0.5000	0.9629						
	$[Li]_{16d}$	0.5000	0.0276						
	$[Al]_{16d}$	0.5000	0.0095						
	$[O]_{32e}$	0.2604(3)	1.0000						
$y = 0.05$	$[Li]_{8a}$	0.1250	1.0000	8.2281(4)	1.9181(6)	1.9801(3)	6.36	8.68	3.13
	$[Mn]_{16d}$	0.5000	0.9491						
	$[Li]_{16d}$	0.5000	0.0277						
	$[Al]_{16d}$	0.5000	0.0236						
	$[O]_{32e}$	0.2615(4)	1.0000						
$y = 0.08$	$[Li]_{8a}$	0.1250	1.0000	8.2229(5)	1.9470(4)	1.9646(3)	6.45	8.71	3.23
	$[Mn]_{16d}$	0.5000	0.9333						
	$[Li]_{16d}$	0.5000	0.0278						
	$[Al]_{16d}$	0.5000	0.0389						
	$[O]_{32e}$	0.2626(3)	1.0000						
$y = 0.1$	$[Li]_{8a}$	0.1250	1.0000	8.2193(5)	1.9762(3)	1.9479(1)	6.55	8.64	3.17
	$[Mn]_{16d}$	0.5000	0.9243						
	$[Li]_{16d}$	0.5000	0.0276						
	$[Al]_{16d}$	0.5000	0.0481						
	$[O]_{32e}$	0.2638(2)	1.0000						

[a] M indicates the elements occupied in 16d site such as Mn, Li, and Al; R_p is the profile factor; R_{wp} is the weighted profile factor; χ^2 is the goodness of fit.

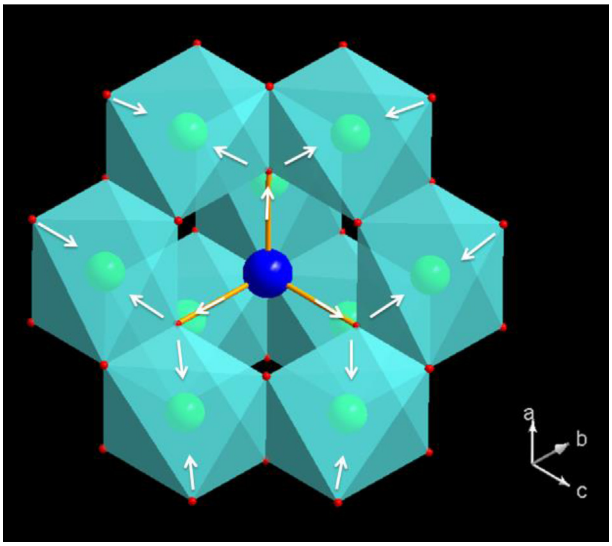

Fig. 7. Schematic illustration of ball-stick polyhedron: the concerted expansion of LiO_4 tetrahedron and contraction of MO_6 octahedron (green–$[Li]_{8a}$, blue–$[M]_{16d}$, red–$[O]_{32e}$). (For interpretation of the references to color in this figure legend, the reader is referred to the web version of this article).

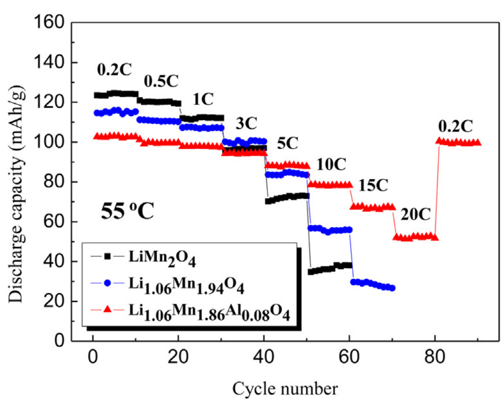

Fig. 8. Discharge rate capability of the $LiMn_2O_4$, $Li_{1.06}Mn_{1.94}O_4$ and $Li_{1.06}Mn_{1.86}Al_{0.08}O_4$ samples at 55 °C.

85.4, 91.2 and 89.1 mAh g^{-1} after 200 cycles, respectively. It is found that Al-doped samples have the improved elevated-temperature cycling stability compared with the undoped one, implying that the Al-doped samples have a higher structural stability.

Table 3
Impedance parameters of the $LiMn_2O_4$, $Li_{1.06}Mn_{1.94}O_4$ and $Li_{1.06}Mn_{1.86}Al_{0.08}O_4$ samples after 1 and 200 cycles at 55 °C.

Sample	R_1 (Ω)		R_{sf} (Ω)		R_{ct} (Ω)	
	1st	200th	1st	200th	1st	200th
$LiMn_2O_4$	6.0	8.2	17.6	163.8	22.9	472.5
$Li_{1.06}Mn_{1.94}O_4$	7.1	10.5	18.5	90.9	36.2	204.1
$Li_{1.06}Mn_{1.86}Al_{0.08}O_4$	7.3	10.8	18.7	67.3	39.5	120.2

The structural properties of the $Li_{1.06}Mn_{1.94-y}Al_yO_4$ samples are critical to the resultant enhanced electrochemical performance. Thus, careful characterization of Rietveld refinement of XRD diffractograms were performed to further understand their crystallographic properties, linking to Li/Mn/Al location and content, oxygen positional parameter, and lattice parameter. In the refinements, a pseudo-Voigt function and a linear interpolation between the set background points with refinable heights were used to define the profile shape and the background, respectively. Except for the occupancy parameters of the ions, which were fixed at the nominal composition, all other parameters such as scale factor, zero correction, background, half-width parameters, the mixing parameters, lattice parameters, positional coordinates, and thermal parameters were varied in the course of refinement. Fig. 5 depicts the Rietveld fit for the $Li_{1.06}Mn_{1.94-y}Al_yO_4$ samples using a cubic spinel in the *Fd-3m* space group. As observed the expanded 2θ region in Fig. 6, the main diffraction peaks of the patterns shifts to a higher angle as more Al-dopant is added, indicating a decrease of lattice size of the unit cell. The refined parameters are summarized in Table 2.

As Table 2 shows, a reasonable fit between the observed and the calculated data was obtained with good agreement factors. The XRD patterns of the pristine and Al-doped $Li_{1.06}Mn_{1.94}O_4$ samples, as shown in Fig. 3, can be assigned to the *Fd-3m* space group, without any impurity phases, indicating that Al-doping does not affect the formation of a cubic spinel. It also further verifies the abovementioned statement of the additional Li has been incorporated into the spinel lattice of the 16d site, which is usually occupied by the Mn atoms for the $LiMn_2O_4$ samples. The refinement results also indicate the contraction of the unit cell with Al-doping, corresponding to the values obtained by Le Bail fitting. An interesting result comes from the difference in the interatomic distance. While the $[Li]_{8a}$-$[O]_{32e}$ distance has noticeably increased upon Al-doping, taking $y = 0$ and 0.1 for examples, namely, the $Li_{1.06}Mn_{1.94}O_4$ and $Li_{1.06}Mn_{1.84}Al_{0.1}O_4$ samples, their respective $[Li]_{8a}$-$[O]_{32e}$ distances are 1.8346(5) Å and 1.9762(9) Å, and the $[M]_{16d}$-$[O]_{32e}$ distance (M indicates the elements occupied in 16d

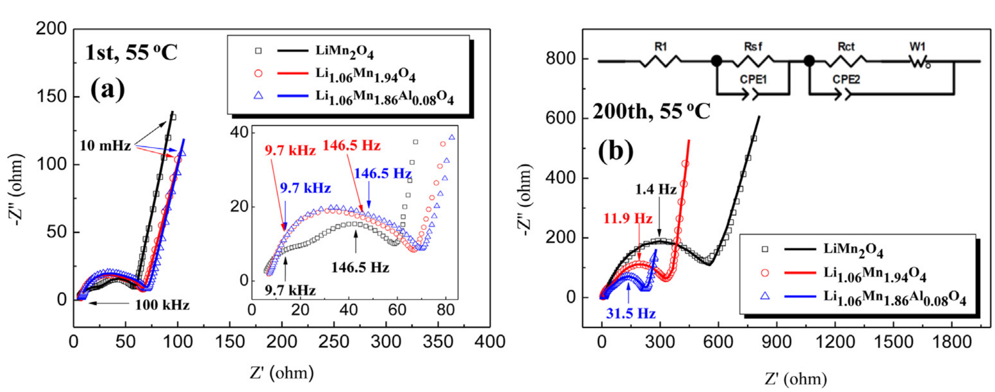

Fig. 9. EIS spectra of the $LiMn_2O_4$, $Li_{1.06}Mn_{1.94}O_4$ and $Li_{1.06}Mn_{1.86}Al_{0.08}O_4$ samples at 55 °C, (opened) recorded after (a) 1 and (b) 200 charge–discharge cycles; (solid line) simulated curves using the equivalent circuit in inset.

site such as Mn, Li, and Al.) has simultaneously decreased from 2.0321(3) Å to 1.9479(7) Å, eventually resulting in a unit cell contraction, from 8.2352(9) Å to 8.2193(5) Å. The concomitant changes of both $[Li]_{8a}$-$[O]_{32e}$ and $[M]_{16d}$-$[O]_{32e}$ distances are interesting for the following: on the one hand, the increase in volume of the LiO_4 tetrahedron suggests the possible to utilize the fast electrochemical kinetics [30]; on the other hand, the contraction of the MO_6 octahedron implies that the spinel-framework can be tightened by Al-doping, which possibly leads to high capacity retention under repeated charge–discharge cycles.

The ball-stick LiO_4 tetrahedral and MO_6 octahedral polyhedrons described in Fig. 7 schematize the concepts addressed above. The white arrows point out the concerted expansion of a LiO_4 tetrahedron and contraction of neighboring MO_6 octahedrons. Since the LiO_4 tetrahedral sites share corners with the MO_6 octahedral sites, and Li^+ ion diffusion occurs through the empty tetrahedron and

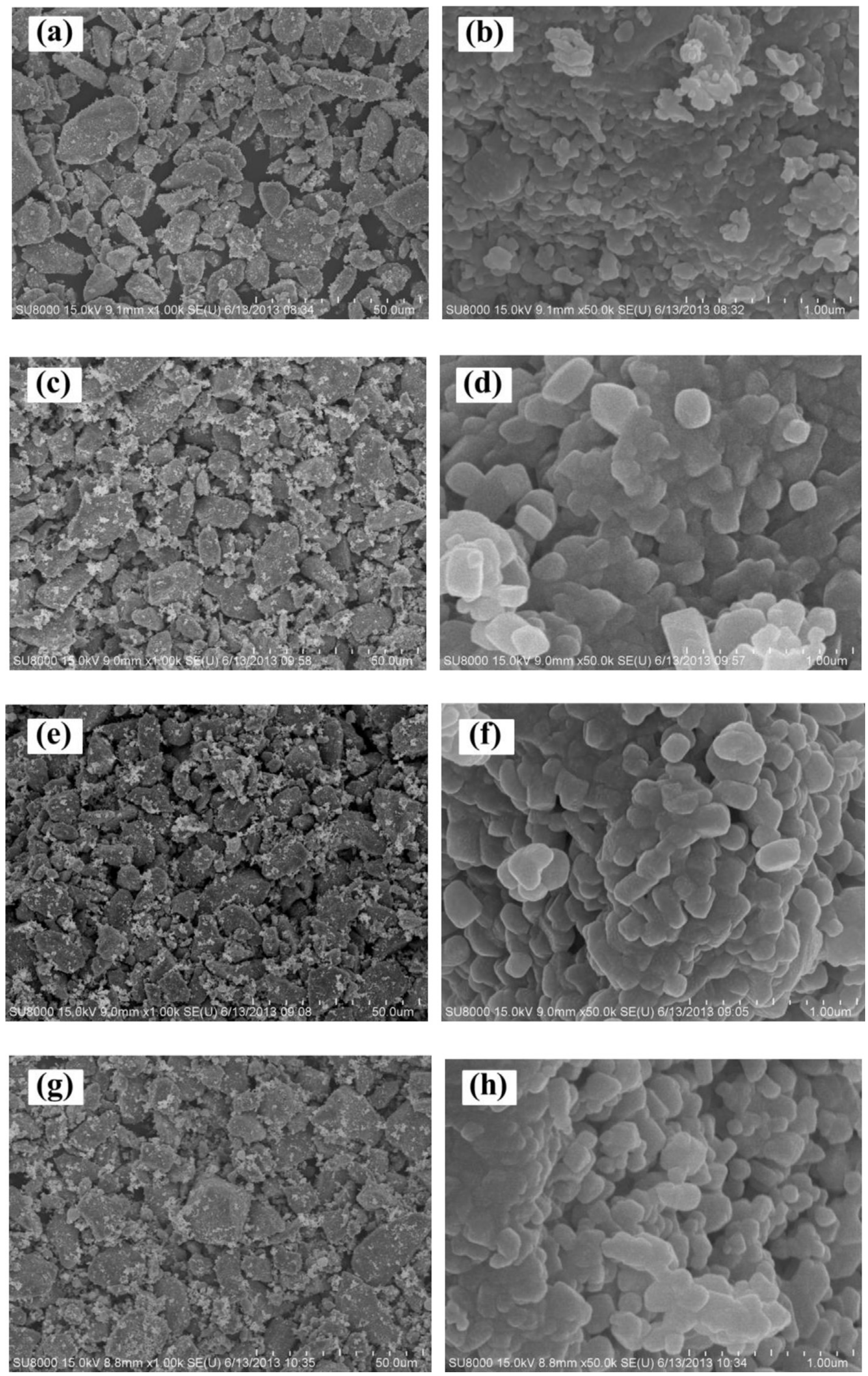

Fig. 10. SEM micrographs of samples: (a–b) electrolytic MnO_2 reagent, (c–d) $LiMn_2O_4$, (e–f) $Li_{1.06}Mn_{1.94}O_4$, and (g–h) $Li_{1.06}Mn_{1.86}Al_{0.08}O_4$, magnified 1000 and 50000 times, respectively.

octahedron interconnected with one another by common faces and edges, the expansion of tetrahedra implies the possible to facilitate a fast electrochemical process, leading to optimal rate performance, even at elevated temperatures.

Fig. 8 compares the discharge capacities of $LiMn_2O_4$, $Li_{1.06}Mn_{1.94}O_4$ and $Li_{1.06}Mn_{1.86}Al_{0.08}O_4$ samples at different C-rates. The $LiMn_2O_4$ sample delivers the greatest capacity of about 125 mAh g^{-1} at 0.2 C, has severely decreased with C-rates. On the other hand, the sensitivity of capacity to C-rates for the $Li_{1.06}Mn_{1.94}O_4$ sample has suppressed. For the $Li_{1.06}Mn_{1.86}Al_{0.08}O_4$ sample, the C-rate dependence of the capacity has further weakened, which is obtained the greatest capacities at 5, 10, 15, and 20 C, the corresponding capacities are about 88, 79, 67 and 52 mAh g^{-1}, respectively. From 0.2 C to 10 C, the capacity reductions of $LiMn_2O_4$, $Li_{1.06}Mn_{1.94}O_4$ and $Li_{1.06}Mn_{1.86}Al_{0.08}O_4$ samples are approximately 71%, 52% and 23%, respectively. It should be noted that when the current rate is decreased from 20 C to 0.5 C, the discharge capacity of $Li_{1.06}Mn_{1.86}Al_{0.08}O_4$ can be recovered to around 100 mAh g^{-1}, indicates its good reversibility upon cycling. As a result, the $Li_{1.06}Mn_{1.86}Al_{0.08}O_4$ sample shows the greatest high-rate performance, proving the effectiveness of Li, Al co-doping under high-rate conditions at elevated temperatures.

In order to investigate the electrochemical behavior of the $LiMn_2O_4$, $Li_{1.06}Mn_{1.94}O_4$ and $Li_{1.06}Mn_{1.86}Al_{0.08}O_4$ samples at the electrode/electrolyte interface in detail, EIS measurements were carried out. All of the samples were measured with cycling at the fully discharged state, as described in Fig. 9. Nyquist plots indicate that the depressed semicircles of all of the samples after 1 cycle are enlarged after 200 cycles, and frequency values are denoted for a few typical data points. Using the equivalent circuit in the inset of Fig. 9(b), where R_1 is the solution resistance, R_{sf} and CPE_1 represent the resistance and capacitance the surface film covered electrode particles, R_{ct} and CPE_2 represent the charge-transfer resistance and double-layer capacitance, W_1 is the Li diffusion resistance in the crystal lattice [9,31], characteristic parameters were extracted in Table 3. It can be observed that both of the enlarged R_{sf} and R_{ct} for $LiMn_2O_4$ have been alleviated by Li-doping, which has further relieved for the $Li_{1.06}Mn_{1.86}Al_{0.08}O_4$ sample. It probably thanks to the better structure-stabilization of $Li_{1.06}Mn_{1.86}Al_{0.08}O_4$, leading to a less dissolution of Mn, whereby a smaller increase in impedance upon cycling is achieved.

3.3. Morphological features

Additionally, Fig. 10 exhibits the micrographs of SEM, and there is hardly any difference among the $LiMn_2O_4$, $Li_{1.06}Mn_{1.94}O_4$ and $Li_{1.06}Mn_{1.86}Al_{0.08}O_4$ samples. All of the samples show a good crystallinity and a highly aggregated morphology, namely, the secondary micrometer-sized particles consist of aggregated primary sub-micron particles, all of which faithfully inherit the initial surface structure of the electrolytic MnO_2 reagent. Besides, the $LiMn_2O_4$, $Li_{1.06}Mn_{1.94}O_4$ and $Li_{1.06}Mn_{1.86}Al_{0.08}O_4$ samples have tap-densities as high as 1.82, 1.82 and 1.80 g cm^{-3}, respectively. The median sizes D50 of these three samples are 10.1, 9.9 and 9.6 μm, respectively.

4. Conclusions

In summary, the electrochemical performance of $Li_{1+x}Mn_{2-x-y}Al_yO_4$ ($0 \le x \le 0.12$, $0 \le y \le 0.1$) was investigated and correlated Rietveld refinement analysis of the structural factors was addressed. The decrease of a unit cell dimension by Li, Al co-substitution, accompanied by the expansion of LiO_4 tetrahedron and contraction of MO_6 octahedron, resulted in an improvement in high-rate performance and a better structure-stabilization, respectively. For the optimized composition ($Li_{1.06}Mn_{1.86}Al_{0.08}O_4$), a superior capacity retention ratio of 90% after 200 cycles at 0.5 C at 55 °C (initial value is 102 mAh g^{-1}), and a capacity as high as 88 mAh g^{-1} upon cycling at 10 C at 55 °C, as well as a lower impedance than that of the pristine $LiMn_2O_4$ were obtained. Therefore, the excellent elevated-temperature electrochemical performance will promote the development of $LiMn_2O_4$ cathode materials to meet the large-scale application requirements of high-performance LIBs.

Acknowledgment

We acknowledge the National Natural Science Foundation of China (Grant No. 21273058), China Postdoctoral Science Foundation (Grant No. 2012M520731), Heilongjiang Postdoctoral Financial Assistance (LBH-Z12089) for their financial support.

References

[1] P.G. Bruce, S. Bruno, T.M. Jean, Angew. Chem. Int. Ed. 47 (2008) 2930–2946.
[2] M.R. Palacin, Chem. Soc. Rev. 38 (2009) 2565–2575.
[3] B. Dunn, H. Kamath, J.M. Tarascon, Science 334 (2011) 928–935.
[4] O.K. Park, Y. Cho, S. Lee, H.C. Yoo, H.K. Song, J. Cho, Energy Environ. Sci. 4 (2011) 1621–1633.
[5] K.M. Shaju, P.G. Bruce, Chem. Mater. 20 (2008) 5557–5562.
[6] K.Y. Chung, K.B. Kim, Electrochim. Acta 49 (2004) 3327–3337.
[7] S.R. Das, I.R. Fachini, S.B. Majumder, R.S. Katiyar, J. Power Sources 158 (2006) 518–523.
[8] T.D. Sparks, A. Gurlo, D.R. Clarke, J. Mater. Chem. 22 (2012) 4631–4636.
[9] S. Lee, Y. Cho, H.K. Song, K.T. Lee, J. Cho, Angew. Chem. Int. Ed. 51 (2012) 8748–8752.
[10] W.K. Kim, D.W. Han, W.H. Ryu, S.J. Lim, H.S. Kwon, Electrochim. Acta 71 (2012) 17–21.
[11] M. Prabu, M.V. Reddy, S. Selvasekarapandian, S. Admas, K.P. Loh, G.S. Rao, B.V. Chowdari, J. Electrochem. Soc. 160 (2013) A3144–A3147.
[12] W. Liu, J. Liu, K. Chen, S. Ji, Y. Wan, Y. Zhou, Y. Li, Chem. A Eur. J. 20 (2014) 824–830.
[13] C. Sigala, A.L.G. La Salle, Y. Piffard, D. Guyomard, J. Electrochem. Soc. 148 (2001) A812–A818.
[14] H. Shigemura, H. Sakaebe, H. Kageyama, H. Kobayashi, A.R. West, R. Kanno, M. Tabuchi, J. Electrochem. Soc. 148 (2001) A730–A736.
[15] R. Thirunakaran, N. Kalaiselvi, P. Periasamy, B.R. Babu, N.G. Renganathan, N. Muniyandi, M. Raghavan, Ionics 7 (2001) 187–191.
[16] S. Mandal, R.M. Rojas, J.M. Amarilla, P. Calle, N.V. Kosova, V.F. Anufrienko, J.M. Rojo, Chem. Mater. 14 (2002) 1598–1605.
[17] Y.J. Wei, L.Y. Yan, C.Z. Wang, X.G. Xu, F. Wu, G. Chen, J. Phys. Chem. B 108 (2004) 18547–18551.
[18] A. Sulochana, R. Thirunakaran, A. Sivashanmugam, S. Gopukumar, J.I. Yamaki, J. Electrochem. Soc. 155 (2008) A206–A210.
[19] C.L. Tan, H.J. Zhou, W.S. Li, X.H. Hou, D.S. Lü, M.Q. Xu, Q.M. Huang, J. Power Sources 184 (2008) 408–413.
[20] S. Guo, S. Zhang, X. He, W. Pu, C. Jiang, C. Wan, J. Electrochem. Soc. 155 (2008) A760–A763.
[21] M.V. Reddy, S.S. Manoharan, J. John, B. Singh, G.S. Rao, B.V.R. Chowdari, J. Electrochem. Soc. 156 (2009) A652–A660.
[22] W.H. Ryu, J.Y. Eom, R.Z. Yin, D.W. Han, W.K. Kim, H.S. Kwon, J. Mater. Chem. 21 (2011) 15337–15342.
[23] Y. Mizuno, N. Zettsu, H. Nagaki, S. Komine, K. Kami, K. Yubuta, K. Teshima, CrystEngComm 16 (2014) 1157–1162.
[24] W. Lu, I. Belharouak, S.H. Park, Y.K. Sun, K. Amine, Electrochim. Acta 52 (2007) 5837–5842.
[25] A.C. Larson, R.B. Von Dreele, General Structure Analysis System (GSAS) LAUR, 2004.
[26] N. Yabuuchi, M. Yano, S. Kuze, S. Komaba, Electrochim. Acta 82 (2012), 296–231.
[27] L. Xiong, Y. Xu, T. Tao, J. Song, J.B. Goodenough, J. Mater. Chem. 22 (2012) 24563–24568.
[28] M. Kopec, J.R. Dygas, F. Krok, A. Mauger, F. Gendron, B. Jaszczak-Figiel, C.M. Julien, Chem. Mater. 21 (2009) 2525–2533.
[29] H.T. Chung, S.T. Myung, T.H. Cho, J.T. Son, J. Power Sources 97 (2001) 454–457.
[30] M. Winter, J.O. Besenhard, M.E. Spahr, P. Novak, Adv. Mater. 10 (1998) 725–763.
[31] Q.C. Zhuang, T. Wei, L.L. Du, Y.L. Cui, L. Fang, S.G. Sun, J. Phys. Chem. C 114 (2010) 8614–8621.